

Patient-Specific Bioimplants and Reconstruction Plates for Mandibular Defects: Production Workflow and In Vivo Large Animal Model Study

Kasper Dienel, Ahmed Abu-Shahba, Roman Kornilov, Roy Björkstrand, Bas van Bochove, Johanna Snäll, Tommy Wilkman, Karri Mesimäki, Anna Meller, Jere Lindén, Anu Lappalainen, Jouni Partanen, Riitta Seppänen-Kajjansinkko, Jukka Seppälä,* and Bettina Mannerström

A major challenge with extensive craniomaxillofacial bone reconstruction is the limited donor-site availability to reconstruct defects predictably and accurately according to the anatomical shape of the patient. Here, patient-specific composite bioimplants, consisting of cross-linked poly(trimethylene carbonate) (PTMC) networks and β -tricalcium phosphate (β -TCP), are tested in vivo in twelve Göttingen minipigs in a large mandibular continuity defect model. The 25 mm defects are supported by patient-specific titanium reconstruction plates and receive either osteoconductive composite bioimplants (PTMC+TCP), neat polymer network bioimplants (PTMC), autologous bone segments (positive control), or are left empty (negative control). Postoperatively, defects treated with bioimplants show evident ossification at 24 weeks. Histopathologic evaluation reveals that neat PTMC bioimplant surfaces are largely covered with fibrous tissue, while in the PTMC+TCP bioimplants, bone attached directly to the implant surface shows good osteoconduction and histological signs of osteoinductivity. However, PTMC+TCP bioimplants are associated with high incidence of necrosis and infection, possibly due to rapid resorption and/or particle size of the used β -TCP. The study highlights the importance of testing bone regeneration implants in a clinically relevant large animal model and at the in situ reconstruction site, since results on small animal models and studies in nonloadbearing areas do not translate directly.

1. Introduction

Reconstruction of bone defects caused by trauma, infection, tumor resection, or skeletal abnormalities is challenging, requiring extensive preoperative planning and demanding surgical procedures in order to restore both form and function of the defect site.^[1] In particular, craniomaxillofacial (CMF) reconstructions are demanding due to the individual, complex shape of the face and jaw functions. Current treatment relies on autologous bone, however, the method is affected by donor-site morbidity and the limited control over shaping the bone graft. Subsequently, advances in the fields of materials science and tissue engineering are anticipated to provide novel reconstructive solutions. Alloplastic synthetic polymers have a great potential for reconstructing bone defects, as they feature full control over implant engineering aspects, including material properties, biological activity, and implant geometry.^[2]


Patient-specific implants (PSI) enable optimal functional reconstruction while reducing the length of the surgical

K. Dienel, B. van Bochove, J. Seppälä
Polymer Technology, School of Chemical Engineering
Aalto University
Espoo 02150, Finland
E-mail: jukka.seppala@aalto.fi

A. Abu-Shahba, R. Kornilov, J. Snäll, R. Seppänen-Kajjansinkko,
B. Mannerström
Department of Oral and Maxillofacial Diseases
University of Helsinki and Helsinki University Hospital
Helsinki 00290, Finland

A. Abu-Shahba
Department of Oral and Maxillofacial Surgery
Faculty of Dentistry
Tanta University
Tanta 31773, Egypt

R. Björkstrand, J. Partanen
Department of Mechanical Engineering
Aalto University
Espoo 02150, Finland

 The ORCID identification number(s) for the author(s) of this article can be found under <https://doi.org/10.1002/mabi.202100398>

© 2022 The Authors. Macromolecular Bioscience published by Wiley-VCH GmbH. This is an open access article under the terms of the Creative Commons Attribution-NonCommercial-NoDerivs License, which permits use and distribution in any medium, provided the original work is properly cited, the use is non-commercial and no modifications or adaptations are made.

DOI: 10.1002/mabi.202100398

procedure, likely shortening the time needed for healing, guaranteeing precise anatomical shape, and thus, optimally obviating the need for additional surgeries. PSIs can be designed virtually based on data from computed tomography (CT) imaging, followed by additive manufacturing (AM) of implants. This work aimed to develop load-bearing bone regenerative therapies utilizing patient-specific osteoconductive bioimplants that restore CMF defects in a precise and predictable manner. Therefore, our study set out to reconstruct a large mandibular defect in a mechanically demanding area. Reconstruction of such defects is challenging and has a significant impact on the oral functions, affecting the patient's nutrition, psychosocial well-being, esthetics, and quality of life.^[1,3,4] Minipigs were chosen for the in vivo study as the size, bone regeneration rate, and temporomandibular joint movements are comparable to those in humans.^[5]

The scaffold performance is dependent on constituent biomaterials^[2,6] and the scaffold architecture.^[7,8] In biomaterials research, the field advances towards improving functionality, optimizing mechanical properties and degradation kinetics, and providing versatile solutions for better customization.^[9,2] Within this work we manufactured large bone regeneration scaffolds (bioimplants) by vat photopolymerization of composite resins consisting of three-armed methacrylate functionalized poly(trimethylene carbonate) (PTMC-tMA) and osteoconductive β -tricalcium phosphate (β -TCP). Such cross-linked PTMC-tMA-network bioimplants show clinically advantageous properties including biocompatibility and osteoconductivity,^[10–12] enzymatic surface erosion,^[13] and readiness to print in complex shapes and architectures at high resolution.^[14] In addition to bioimplants, patient-specific titanium reconstruction plates are needed to support the defect site. As the supporting plate is separate from the bioimplant, it may eventually be removed. The most common implant material used in AM is medical grade titanium, Ti-6Al-4V. Several examples and applications of such implants as load bearing components exist showing achieved improvements in operation.^[15–17]

T. Wilkman, K. Mesimäki
Department of Oral and Maxillofacial Surgery
Helsinki University Hospital
Helsinki 00290, Finland

A. Meller
Laboratory Animal Center
HiLIFE

University of Helsinki
Helsinki 00790, Finland

J. Lindén
Department of Veterinary Biosciences
Faculty of Veterinary Medicine
University of Helsinki
Helsinki 00790, Finland

J. Lindén
Finnish Centre for Laboratory Animal Pathology
HiLIFE
University of Helsinki
Helsinki 00790, Finland

A. Lappalainen
Department of Equine and Small Animal Medicine, Faculty of Veterinary
Medicine
University of Helsinki
Helsinki 00790, Finland

In this study, we present a complete production workflow for rapid and predictable construction of bone regeneration bioimplants and supporting reconstruction plates for treating bone defects in mechanically demanding areas. This proof-of-concept study was developed to challenge the workflow and the biomaterials performance in a large mandibular continuity defect model in twelve minipigs.

2. Experimental Design and Study Outline

The study consisted of two main parts:

- 1) planning, modelling, fabrication, and characterization of patient-specific osteoconductive bioimplants and supporting titanium plates
- 2) minipig mandibular reconstruction including clinical, radiological and histological evaluation of biomaterial performance.

The results are also presented in this order. A detailed Experimental Section is included at the end of this manuscript.

The outline of the in vivo large animal model study is presented in **Figure 1**. Surgeries were carried out in two stages. In surgery 1, eight weeks before the planned mandibular resection (surgery 2) teeth related to the resection site were extracted to avoid intraoral communication in the second surgery. Two weeks after teeth extraction, the minipigs underwent computed tomography (CT) scan (pre-operative CT (pre-op CT)) for constructing a volumetric anatomy model, based on which the PSIs were modeled and manufactured. Thus, the virtual surgery, fabricating, characterizing, and sterilizing the 12 custom-made bioimplants and reconstruction plates was conducted in six weeks.

In surgery 2, a unilateral 25 mm-long continuity defect was created in the mandible to be supported with a patient-specific titanium reconstruction plate. The defects received either the 3D printed patient-specific bioimplants, modified autologous native bone segments (positive control), or were left empty as negative controls. Two types of bone regeneration scaffolds were manufactured for the study: a biocompatible polymer PTMC-tMA-network only (hereafter referred to as PTMC bioimplants/scaffolds) and a composite of PTMC-tMA-network and osteoconductive β -TCP (hereafter referred to as PTMC+TCP bioimplants/scaffolds). As one minipig was lost between surgery 1 and 2, the resulting 11 minipigs (abbreviated MP 1–12) were randomly assigned into four study groups by blinded allocation (see **Table 1**). Two follow-up CT scans were performed during the study at 6- and 16-weeks postimplantation and the study was terminated 24 weeks postimplantation. At the endpoint a final CT scan was taken, and the reconstructed site was harvested, examined, and prepared for micro-CT (μ CT) analysis and histological processing. Furthermore, the patient-specific reconstruction plates were collected for postimplantation analysis.

3. Results

3.1. Bioimplant and Reconstruction Plate Characterization

Patient-specific bioimplants and reconstruction plates were successfully manufactured for all animals in the limited timeframe

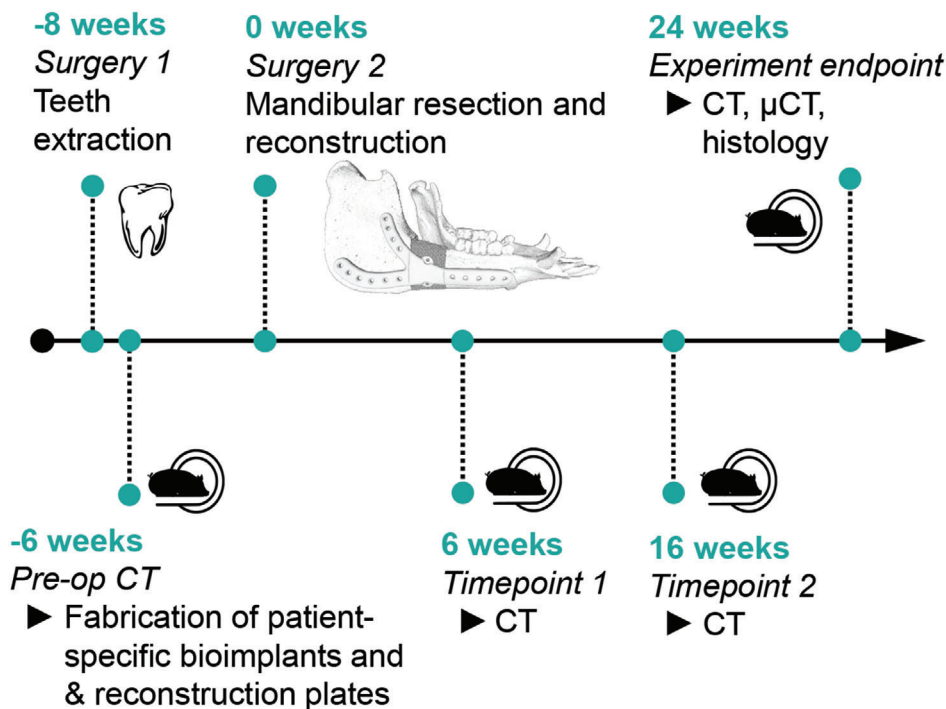


Figure 1. Outline of the study.

Table 1. Study groups. The animals were randomly assigned to each group.

Study group	Nr. of animals	Abbreviations for animals in this group
PTMC	3	MP1, MP2, MP3
PTMC+TCP	4	MP4, MP5, MP12
Empty defect (negative control)	2	MP7, MP8
Bone (positive control)	2	MP10, MP11

of 6 weeks between the pre-op CT and the mandibular resection and implantation (surgery 2). The manufacturing process is described in **Figure 2**.

Images of the manufactured patient-specific bioimplants are shown in **Figure 3** and Figure S2 (Supporting Information). The manufactured PTMC bioimplants deviated on average 0.2 ± 0.2 mm from the 3D design, while PTMC+TCP bioimplants deviated from the design 0.5 ± 0.1 mm. The designed porosity was 71.5% and pore size 800 μ m, while the average porosity for the manufactured bioimplants were $74 \pm 1\%$ for PTMC samples, and $76 \pm 1\%$ for PTMC+TCP samples. These values indicate a high build quality, including excellent feature resolution and uniformity with the 3D model. The full data on bioimplant dimensions can be found in supporting Table S2 in the Supporting Information. Furthermore, the manufacturing consistency was dependable, with only one failed build during manufacturing, which is notable considering the large size of the built structures.

We have previously described the synthesis and characterization of PTMC-tMA,^[14] a brief description and some study specific synthesis results are shown in the Supporting Information. Fur-

thermore, a prototyping table (Table S1, Supporting Information) is included in the Supporting Information describing the development and selection of the vat photopolymerization resin and gyroid design used within this study. The bioimplant design parameters including porosity, pore size and polymer/ceramic ratio were optimized through prototyping based on constraints set by the manufacturing method and the large size of the implant. Finally, interconnected porous implant with a pore size of 800 μ m, porosity 71.5%, and β -TCP content of 40 wt% was chosen. Previous findings^[14] indicated, that a vat photopolymerization resin including 35 wt% β -TCP should be utilized in manufacturing to achieve a final content of around 40 wt% in the built bioimplants. Indeed, thermogravimetric analysis (TGA) of the PTMC+TCP composite bioimplants revealed a β -TCP content of 41 wt% as calculated from the residual mass. Scanning electron microscope (SEM) images of PTMC and PTMC+TCP scaffolds can be seen in Figure 3. These images clearly show the smooth surface of neat PTMC scaffolds, with the layers of the 3D printing clearly visible. In contrast, the surface of the PTMC+TCP scaffolds is covered with spherical β -TCP particles of the size 1–10 μ m.

Images of the manufactured reconstruction plates can be seen in Figure 3 and Figure S3 (Supporting Information). The form and fit of the reconstruction plates matched the anatomy of the jaw, thereby stabilizing the mandibular segments. Positioning hooks were added to guide the correct position on the mandible and resection marks assisted in performing an accurate osteotomy. Some holes were tight since the used narrow screw flange did not allow the use of larger tolerances in manufacturing.

The reconstruction plates were scanned after fabrication and at experiment endpoint to assess for deformations. The found

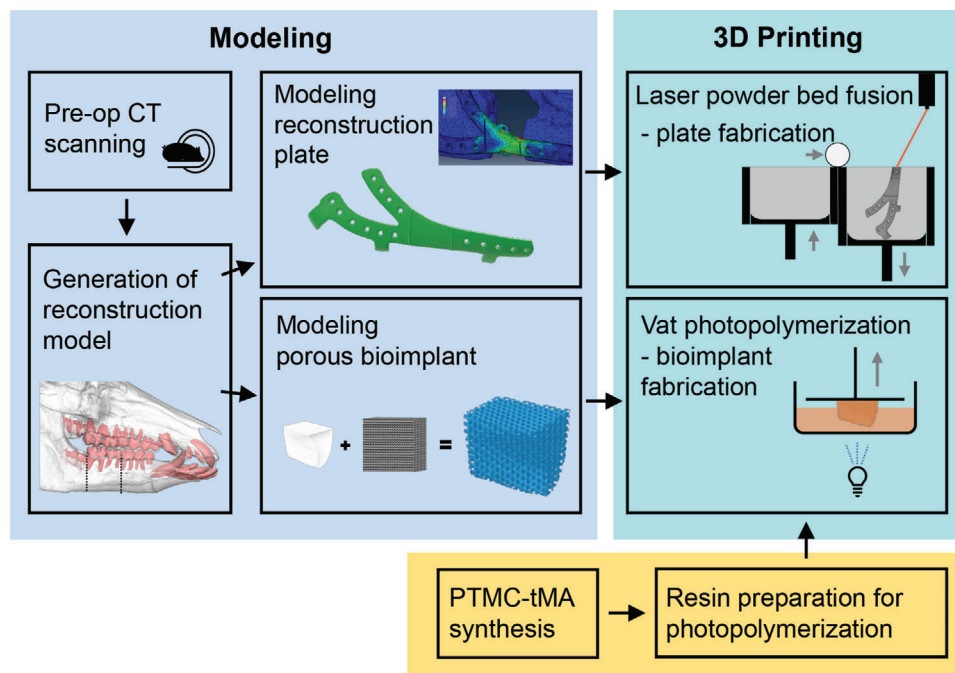


Figure 2. Block diagram describing the manufacturing of custom-made titanium reconstruction plates and bone regeneration bioimplants.

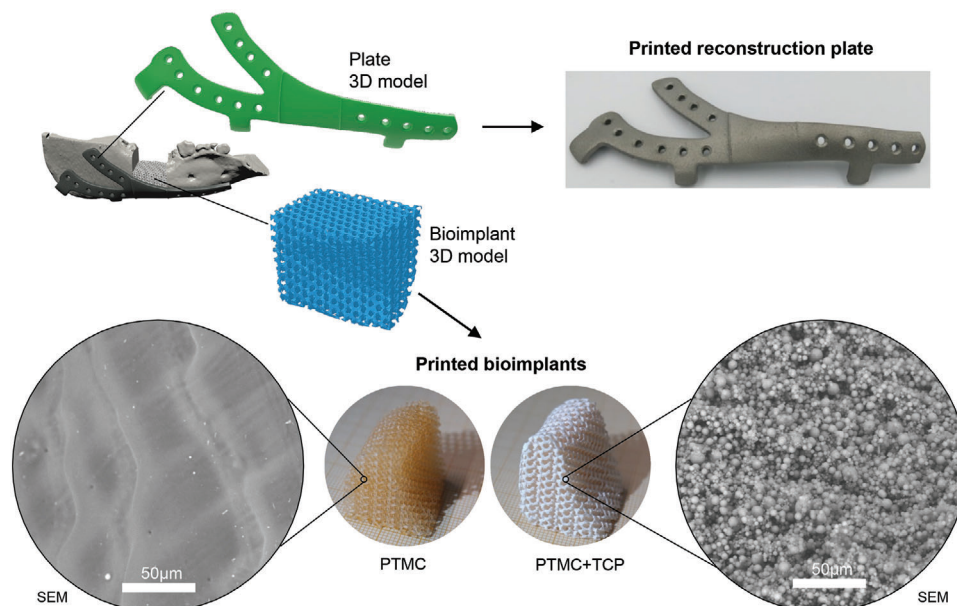


Figure 3. Images of 3D reconstruction model with bioimplant and reconstruction plate STL-files as well as printed implants. SEM images of PTMC and PTMC+TCP bioimplants are included to show the surface morphology of the manufactured samples.

anomalies between different stages were overall very subtle. The main part of deformations is due to manufacturing accuracy since *asBuilt* scans differed from *asDesigned* models typically much more than what the difference between *asBuilt* and *postoperative* scans was. **Figure 4**, presenting an example of the above-mentioned comparisons in the manufacturing orientation, shows that the difference is mainly local. The deviations are most likely due to small collisions with the layer recoating body during

printing or a process interruption of the additive manufacturing equipment. Several plates had their maximum values at the same location, near the Y-branch of the part. Minor production lot specific differences were observed, also pointing at production-based anomalies.

The plate accuracy was within the range of ± 0.3 mm. Geometric difference between *asDesigned* and *asBuilt* (A) was on average 0.07 mm and between *asBuilt* and *postoperative* (B) scans

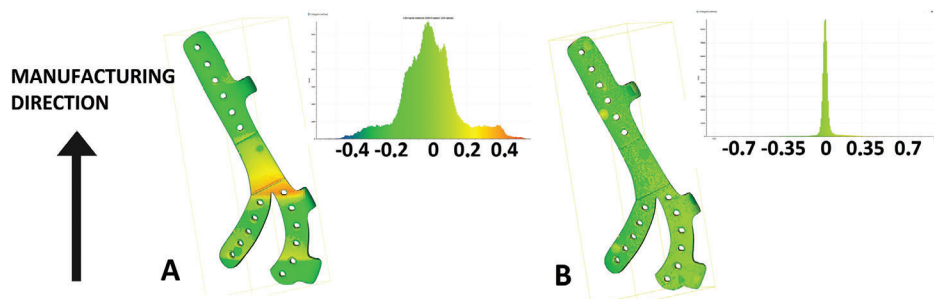


Figure 4. The geometrical differences of minipig MP8 reconstruction plate. Measured by aligning the models on top of each other A) after the manufacturing (*asDesigned* – *asBuilt* models) and B) after the study (*asBuilt* – *postOperative* models). The histograms describe the distribution of point/mesh difference of compared models. The largest geometrical differences were found to origin from manufacturing (A) and actualized mostly in direction of the printed layers (see vertical pattern in A).

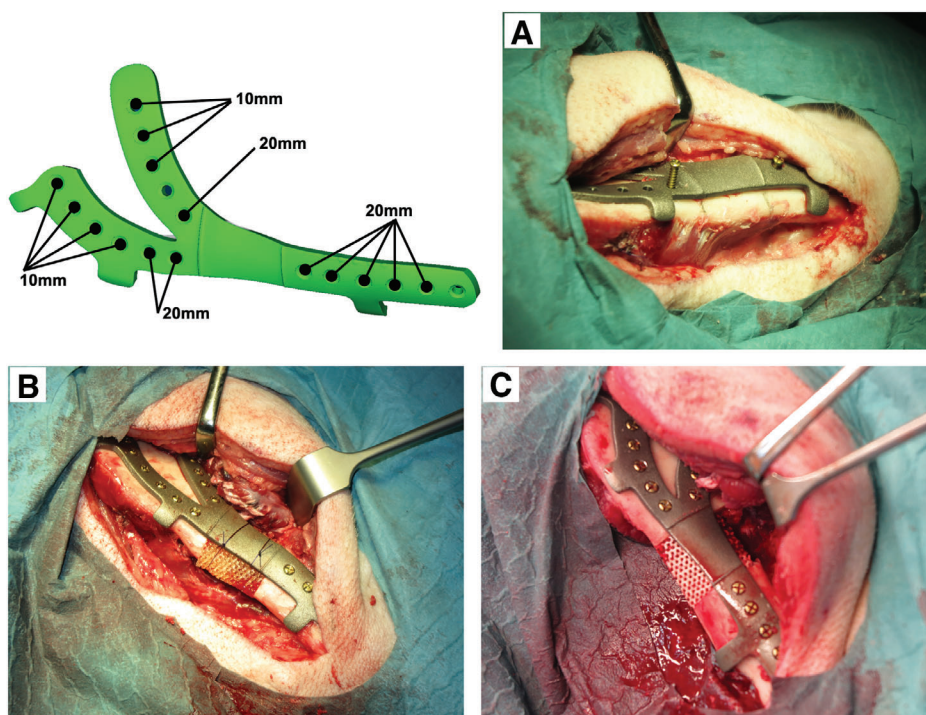


Figure 5. Mandibular resection and reconstruction using bioimplant and plate. A) Marking of the defect according to the resection markings on the custom-made reconstruction plate. B) Reconstruction with PTMC implant. C) Reconstruction with PTMC+TCP bioimplant. Additionally, the figure is showing placement of 10 and 20 mm bicortical screws to stabilize the reconstruction plate.

0.01 mm. As mean value underestimates the maximum deformation, we also report the average gaussian 10% and 90% limit values which were $-0.12/0.27$ mm for A and $-0.03/0.02$ mm for B, which describes better the deformations during the manufacturing and use of the plates.

3.2. Animal Study Results

3.2.1. Results of Surgical Stages and Postoperative Course

All minipigs, except for one (MP9), recovered from the surgical extraction of the defect-related teeth (M1-M3) without complications. In recovery after surgery 1, MP9 developed a diffuse sub-

mucosal ecchymosis with deteriorating clinical condition, which necessitated its euthanasia one week postoperatively. The autopsy revealed that the pig suffered from thrombocytopenic purpura syndrome, previously described for Göttingen minipigs,^[18] which was probably aggravated by the surgery. Two weeks postextraction, the animals underwent pre-op CT under general anesthesia for 3D modelling of the patient-specific bioimplants and supporting titanium reconstruction plates, which also confirmed uneventful healing of the intraoral surgical wounds. The second surgical procedure, the mandibular resection and reconstruction (Figure 5), was carried out by the same surgical team 8 weeks later and proceeded without complications.

After surgery 2, follow-up CT scans of the skull were carried out. At 6 weeks, MP6 had developed a failure of fixation of the

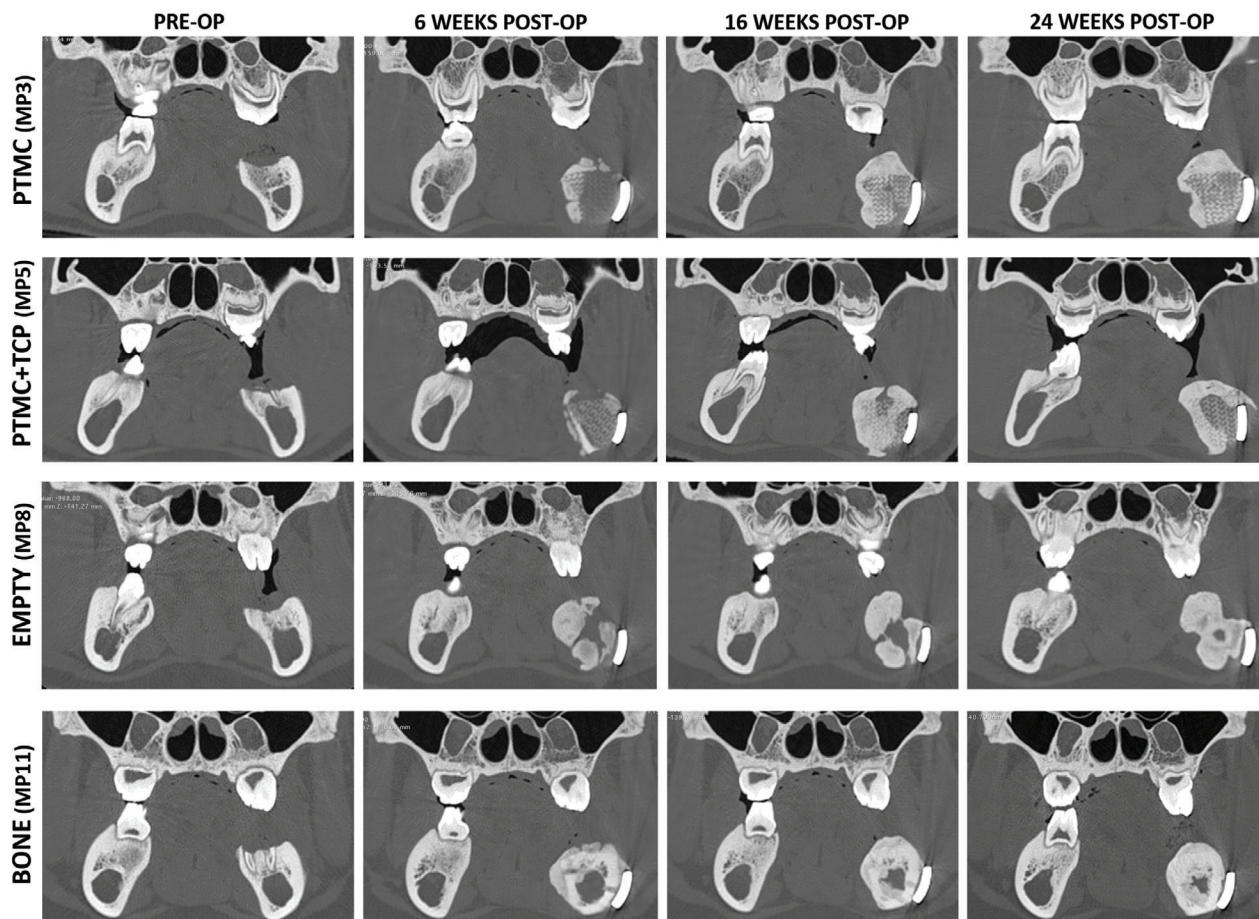


Figure 6. Representative 2D CT images from all study groups; pre-op, 6, 16, and 24 weeks post-OP. Marked new bone formation was seen in all study groups. The mandibular canal appeared to remodel in all groups. PTMC = MP3, PTMC+TCP = MP5, EMPTY = MP8, BONE = MP10.

plate and screws. The exact sequence of events is unclear, possible explanations are slight suboptimal fit of the reconstruction plate anteriorly and the 10 mm screws used being too short for securing the plate. The animal received pain medication and antibiotics, but its condition nevertheless deteriorated, and it was euthanized. Subsequently, a decision was made to perform an extra CT scan on all animals at 6 weeks in addition to the planned 16 and 24 weeks. Radiographically, evident bone formation was observed in all study groups at 6 weeks' CT scan (**Figure 6**). During later follow up, some of the minipigs (MP4, MP5, MP11) developed swelling and fistulas related to the defect site which were managed with fistula cleaning and antibiotic treatment (amoxicillin and clavulanic acid).

At the study endpoint at 24-weeks postreconstruction, all animals were euthanized. Postethanasia, the minipigs were CT scanned after which tissue samples and titanium plates were collected and analyzed.

3.2.2. Computed Tomography Evaluation

Moderate to extensive ossification was visible in the empty defect group already in the 6 weeks' CT scan (Figure 6 CT images

(2D), **Table 2**). At 16 weeks, the defect was completely ossified in MP7 and extensively ossified in MP8. The autologous bone group exhibited large heterogeneity as MP10 had no ossification at 6 weeks, but the defect was completely ossified at 16 weeks, while MP11 in the same group showed severe infection and no ossification at 6 weeks and bone implant dislocation at 16 weeks. In the PTMC and PTMC+TCP groups, ossification was minimal or mild at 6 weeks, and at 16 weeks it varied between mild and moderate in the PTMC group and between minimal and moderate in the PTMC+TCP group. In these two groups, amount of ossification remained similar between 16 and 24 weeks in all animals. Bony callus was seen in all animals at 6 weeks, and it remained rather constant in most animals during the time period. Callus formation was mild or moderate in all except for two animals; MP11 of the autologous bone group had extensive bony callus already at 6 weeks, which remained constant until 24 weeks. MP4 of the PTMC + TCP group had mild bony callus formation at 6 and 16 weeks, but it turned extensive in the 24 weeks scan.

Findings indicating infection were seen in three animals at 6 weeks: two animals (MP4 and MP6) in the PTMC+TCP group and one animal (MP11) in the autologous bone group. In one animal (MP2) in PTMC group, and two animals (MP5 and MP12) in PTMC+TCP group showed mildly increased space between the

Table 2. Evaluation of CT data.

Group	ID	6 weeks				16 weeks				24 weeks			
		Ossif. ^{a)}	Air ^{b)}	Callus ^{c)}	Infec. ^{d)}	Ossif.	Air	Callus	Infec.	Ossif.	Air	Callus	Infec.
PTMC	MP1	2	0	1	0	3	0	1	0	3	0	1	0
PTMC	MP2	1	0	1	1	2	0	2	1	2	0	1	1
PTMC	MP3	1	0	2	0	3	0	1	0	3	0	1	0
PTMC+TCP	MP4	2	1	1	2	3	1	1	2	3	1	3	2
PTMC+TCP	MP5	1	1	1	1	3	1	2	2	3	1	2	2
PTMC+TCP	MP6	1	1	1	2	-	-	-	-	-	-	-	-
PTMC+TCP	MP12	1	2	2	1	1	2	2	1	1	2	2	1
Empty	MP7	3	NA ^{e)}	1	0	5	NA	1	0	5	NA	1	0
Empty	MP8	4	NA	1	0	4	NA	1	0	4	NA	1	0
Bone	MP10	1	NA	2	0	5	NA	0	0	5	NA	1	0
Bone	MP11	0	NA	3	2	NA	NA	3	2	NA	NA	3	3

^{a)} Ossification (Ossif.); 0 = none, 1 = minimal, 2 = mild, 3 = moderate, 4 = extensive, 5 = total ^{b)} Air; 0 = no, 1 = minimal, 2 = yes ^{c)} Callus; 0 = none, 1 = minimal, 2 = moderate, 3 = extensive ^{d)} Infection (Infec.); 0 = no, 1 = space between bone and plate, 2 = marked space between bone and plate, 3 = clear signs of infection ^{e)} NA = not applicable.

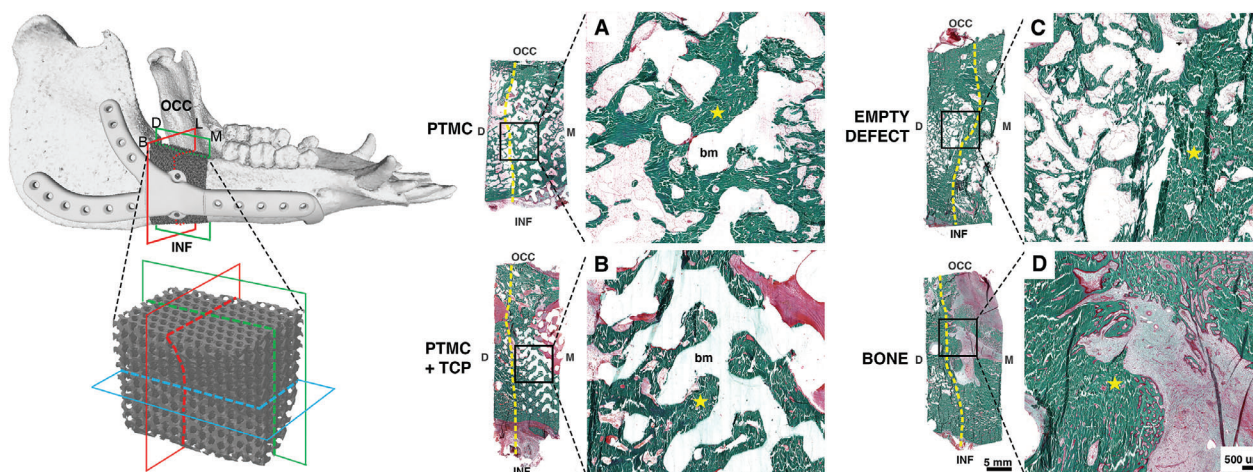


Figure 7. Histology of the defect site. Masson's Trichrome staining on hard tissue sections. A) PTMC, B) PTMC+TCP, C) empty defect, D) autologous bone. In panel (B), fibrotic/necrotic mass is seen in pink (right upper corner) both in overview and in magnification. ★ = new bone formation, bm = bioimplant, dashed line = interface between native bone and defect site. Schematic illustration of defect site and the cutting planes of samples for histological analysis. Scale bar in image.

plate and bone indicating possible infection. At 16 weeks, findings were similar to the previous time point in three animals (MP2, MP4, and MP11), and worsened in one (MP5) from possible infection to infection. One animal was euthanized (MP6) after 6 weeks. At 24 weeks, grading remained similar to the previous time point in all animals. Small air bubbles inside the implant, indicating dryness of the mesh were visible in all scans of the PTMC+TCP group.

3.2.3. Histopathological Evaluation

Three of the four control animals (empty defect and autologous bone) exhibited abundant new bone formation with dense cortical bone occupying large part of the samples (Figure 7C,D). In

contrast, pig MP11 in the autologous bone group showed marked chronic purulent osteomyelitis, abscess formation and sequestration of alveolar bone.

In the PTMC group, in two out of three animals (MP1 and MP3) new bone variably surrounded and moderately infiltrated the bioimplant extending from the defect edges and surrounding periosteum, while fibrous and/or adipose tissue filled the remaining bioimplant mesh (Figures 7A and 8A,C,E). The bone-bioimplant interface was smooth and there was typically no or minimal reaction towards the bioimplant; thin fibrous layer between the biomaterial and the newly formed bone was often present (Figure 8C) and the ingrowing bone showed no interaction with the implant material (Figure 8E). The minimal focal reaction consisted of small numbers of multinucleated giant cells (MGC). The histopathological findings in MP2 differed markedly

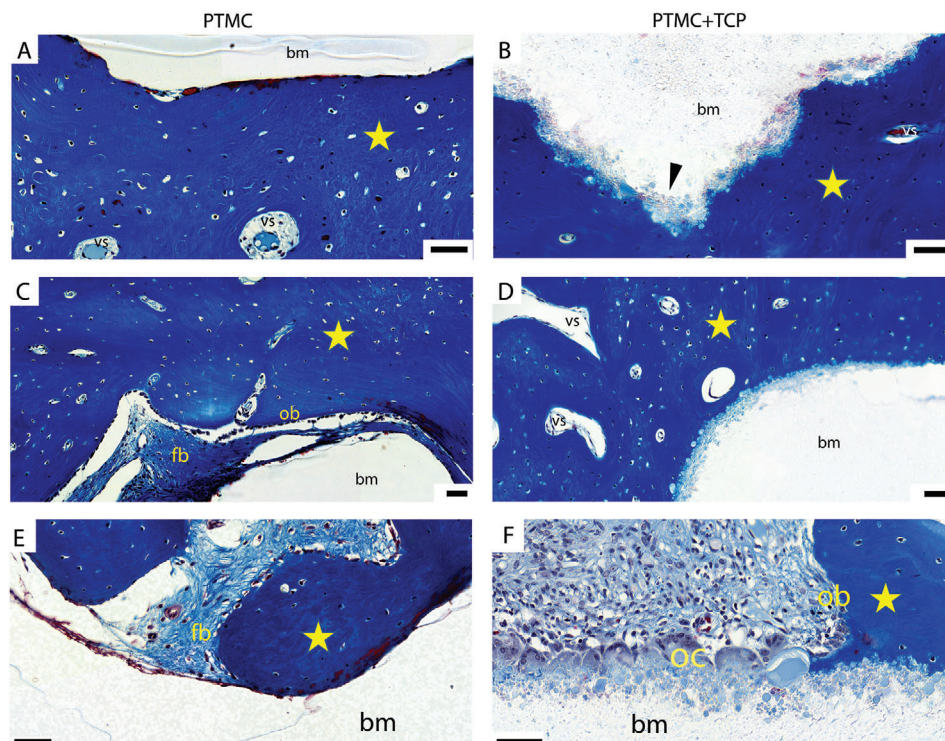


Figure 8. Masson's Trichrome staining on decalcified tissue sections of dense lamellar bone within the scaffolds. A,C,E) PTMC, B,D,F) PTMC+TCP. Mineralized bone attaches tightly to the PTMC+TCP implant surface forming an irregular junction with blue (proteinaceous/mineralized) globules extending into the implant (B; arrow). A thin fibrous layer often lines the scaffold in inner parts of the PTMC bioimplant (C). Osteoclasts pave the way for intramembranous osteogenesis on PTMC+TCP implant surface (F). ★ = new bone formation, bm = bioimplant, fb = fibrous layer, versus = vessels, ob = active osteoblasts, oc = osteoclasts. Scale bar 50 μm .

from the other two animals. It exhibited an inflammatory reaction encircling the bioimplant and generally filling the space inside the bioimplant mesh, and a dense layer of macrophages and MGCs covering the bioimplant surfaces. In the distal-buccal area, bone trabeculae generally covered by osteoblasts invaded part of the bioimplant mesh and formed a network in the core of the inflammatory reaction. Bone formation was moderate occlusally, but very few bone trabeculae were present inferiorly.

All three PTMC+TCP group animals (MP4, MP5, and MP12) sampled at the end of the experiment exhibited qualitatively similar histological findings. Variable amounts of new bone emerged from the edges of the defect and from the surrounding periosteum (Figures 7B and 8B,D), while the rest of the sample area was generally occupied by necrosis and fibrotic capsule that filled the material mesh. The necrotic mass contained large aggregates of gram +/- bacteria, and the bacteria appeared to attach to the bioimplant material in some areas. In MP5 new bone formation covered in general most of the bioimplant areas, whereas in MP4 and MP12 necrosis was more widespread. In MP6 (euthanized at 5 weeks postreconstruction), the histological findings were in general similar to the other PTMC+TCP animals, however, there was marked variation in the extent of necrosis in different parts of the implant, fibrotic capsule formation around the necrotic areas appeared to be less advanced and some granulation tissue was present. In contrast to PTMC, the PTMC+TCP bioimplant material exhibited intensive osteointegration to the new bone that

attached closely to the rough implant surface (Figure 8) forming an irregular junction with small proteinaceous globules extending 20–30 μm into the implant (Figure 8B,D,F). In addition, osteoclast-type cells on the implant surface seemed to induce foci of (intramembranous) osteogenesis and mineralized new bone (Figure 8F).

The animals exhibited no significant macroscopic findings in the autopsy and no significant histopathological findings relating to the implanted materials were detected in selected peripheral organs. In addition, neither the temporomandibular joints (TMJ) on the operated (right) versus control (left) side nor mandibular lymph nodes showed any systematic histopathological differences (Supporting Information; Table S4).

3.2.4. Microcomputed Tomography

After terminating the animal study, the defect area in the mandible was dissected and scanned with μCT . Reconstructions of the defects were created from the data and that was cropped to show the width of the earlier defect (≈ 25 mm). The reconstructed models (Figure 9) revealed that the empty defect group healed well with remodeling bone bridging the defect site. In the autologous bone group, MP10 showed good integration of the implanted autologous bone piece, while in the other minipig (MP11) the bone piece failed to integrate with host tissues and

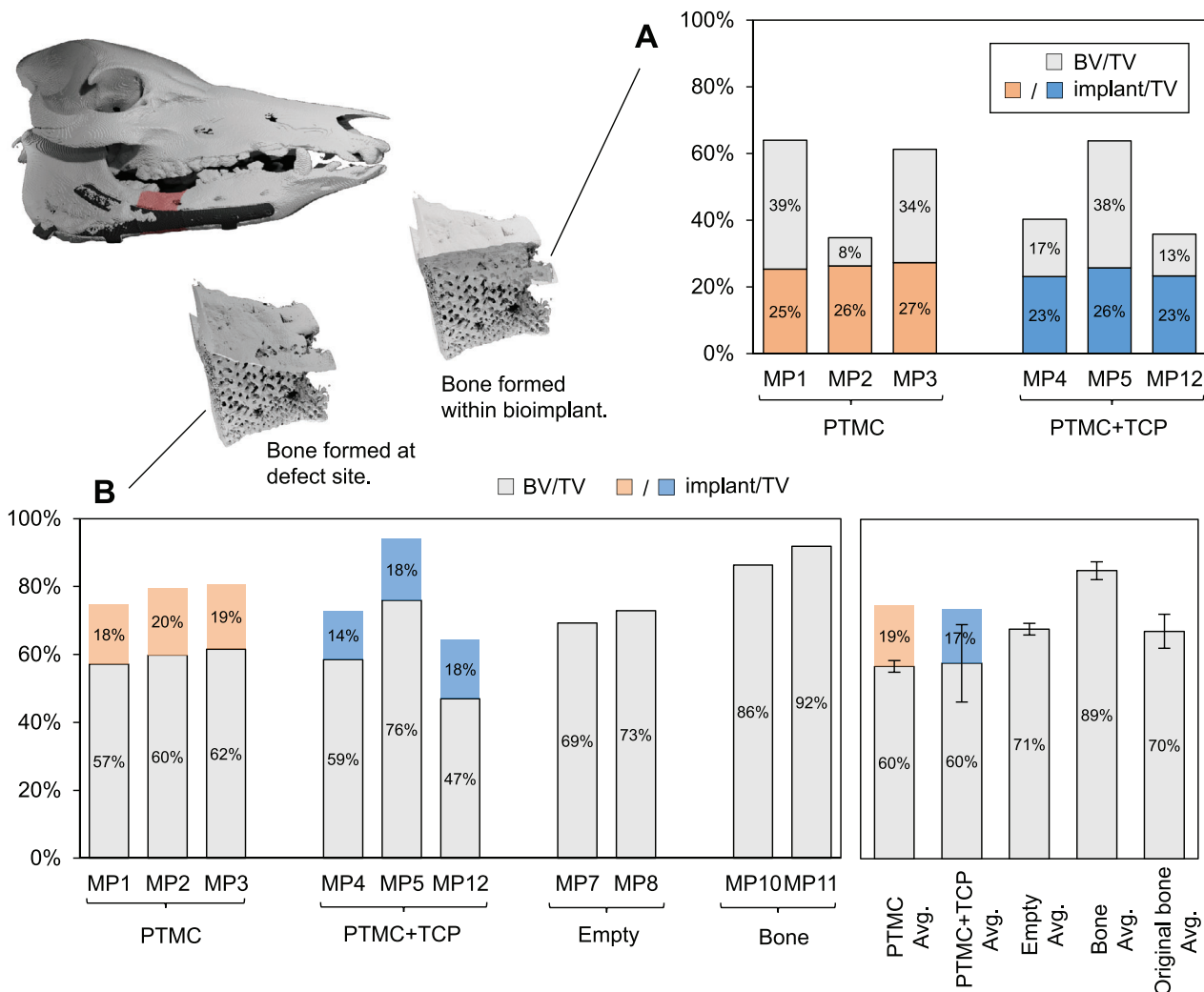


Figure 9. 3D reconstructions of the μ CT data visualizing the bone formed inside the bioimplant (beige) and around the bioimplant (grey) within the defect site. Note that the bioimplant is not visible in the reconstruction.

bony callus was only formed around it. In the animals treated with bioimplants, most exhibited bone formation around the bioimplant subperiosteally and varying bone regeneration within the bioimplant pores. As can be seen in **Figure 10**, three animals showed substantial growth within the bioimplants (34–39% of total volume) while in three animals the growth was less. It should be noted that of the total defect volume $\approx 25\%$ is occupied by the bioimplant as it is 75% porous. No substantial difference can be stated between the two bioimplant groups purely based on the amount of bone infiltrated as the number of animals is low and individual variation is high.

3.3. Manufacturing Workflow Throughput Times and Data Management

As the use of AM in production of the implants increases, challenges in the area of data management and process execution also increase. Moving from one-off cases to routines involving several experts suggest the use of system support. Also, medical de-

vice legislation sets requirements on process and documentation of AM utilization in operations. Managing several patient cases simultaneously and flowing information between stakeholders and expert systems, requires standardized workflows with defined inputs and outputs. Manufacturing workflow throughput times for the PSI designed and fabricated within this study, including data management information, is described in the Supporting Information outlining the workflow performance that an established process can achieve. Through the creation of controlled workflows, including defined procedures, and by systematizing these steps and implementing software solutions, the workflow could be transferred to be semi-automatic and realized in a hospital setting.

4. Discussion

This study set out to develop new patient-specific bone reconstruction methods for large defects in mechanically demanding areas. A complete production cycle was performed following a conceptual workflow to create hybrid reconstruction implants, in-

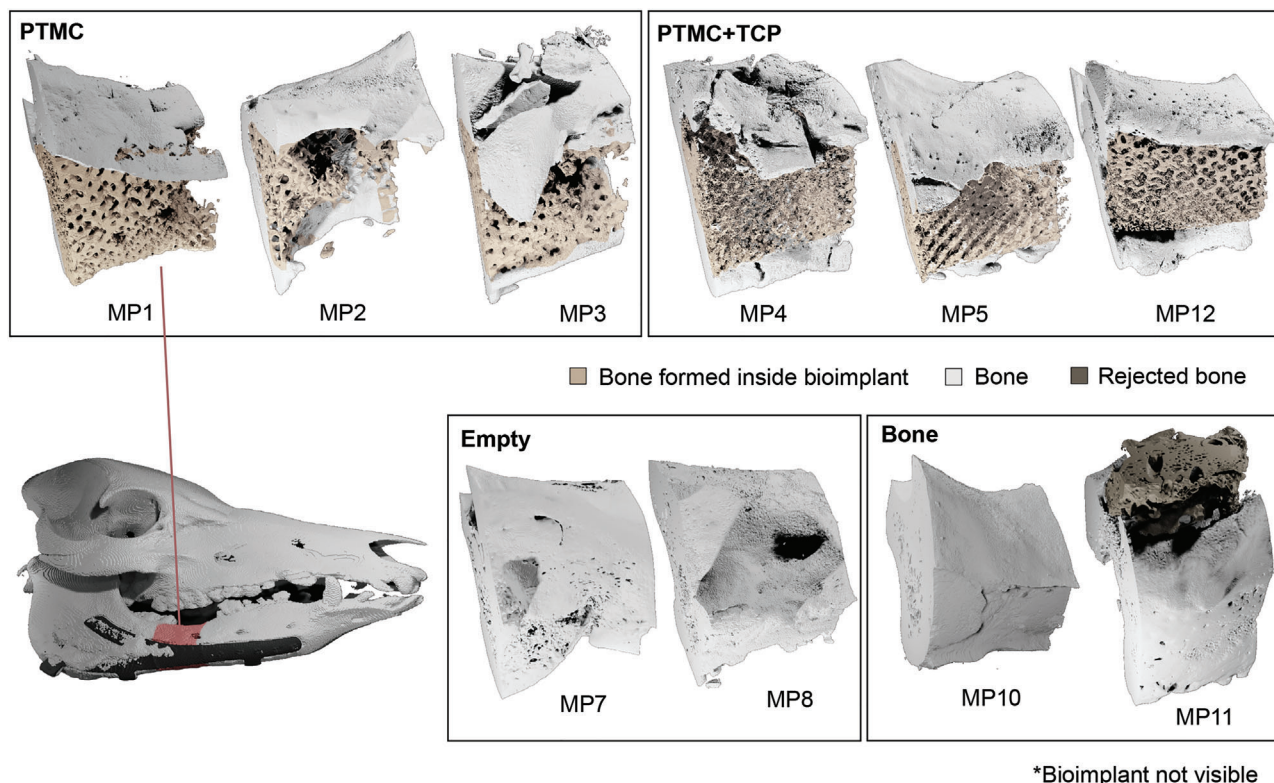


Figure 10. Microcomputed tomography results of the harvested defect site. Graph A shows the bone volume (BV) formed within the total volume (TV) of the bioimplant. As the bioimplants were $\approx 75\%$ porous the implant takes up $\approx 25\%$ of the TV. Graph B shows the bone volume (BV) of the new bone within the whole defect site as a function of the total volume (TV) available at the site, including group mean \pm standard deviation (PTMC $n = 3$, PTMC+TCP $n = 3$, Empty $n = 2$, Bone $n = 2$). The volume ratio taken up by the bioimplant is also in this graph shown for groups PTMC and PTMC+TCP.

cluding bone regeneration bioimplants and supporting titanium plates. The workflow was tested in a proof-of-concept study in twelve minipigs. The following discussion will examine the overall success of the study, concentrating on the performance of the bioimplant and the reconstruction plate.

All animals in this study showed evident ossification of the defect, with some differences between the groups. Specifically, the unexpected incidence of infection in the PTMC+TCP group and the extensive ossification in the empty group are findings that call for more detailed evaluation. The minipig is an appropriate animal model for studying repair of CMF bone defects, owing to its anatomy and bone regeneration rate which is comparable to humans.^[19,20] Still, some differences between pigs and humans may affect the translatability of the results. The bone remodeling rate, defined as the volume of bone turned over per unit volume of tissue per day, is 10% per month in pigs, compared with 3% per month in humans.^[21–23] With these aspects in mind, interpretation of our findings in a human clinical setting demands cautiousness.

As reported in other studies,^[24,25] the defects in our study were covered by periosteum, thus, the bone formation within the defect likely originated for the large part from both the native bone and the periosteum and to a lesser extent due to the osteostimulatory effect of the biomaterial. A conservative design to preserve the periosteum was chosen in this study as complete removal would have risked access into the oral cavity, potentially resulting

in infection. Animal models for the evaluation of calvarial critical size defects (CSD, a defect that will not heal spontaneously) have been well established in the rat, rabbit,^[10] and dog,^[26] however, the size of a CSD for minipigs is still unclear and further investigations will set the foundation for building standards.^[24,25,27–29] In a minipig study to set the limits of a CSD without applying biomaterials or implants, Ma et al.^[30] showed that if periosteal integrity is disrupted in a continuity defect in the body of the mandible, 2 cm is of critical-size, and if the periosteum is left intact, a 6 cm defect is of critical-size. Our study supports this finding, with robust bone formation in the empty defect group, showing that the periosteum has an impact on the healing of a large mandibular defects. This parallels some previous clinical reports.^[31–33]

To efficiently facilitate reconstruction and bone ingrowth, the bioimplant should conform with comprehensive material property and engineering criteria.^[34] The porous design of the bioimplant should be interconnected to allow bone ingrowth throughout the implant, with a large surface area for cell attachment. The pore size should be small enough to support effective pore bridging, however large enough to enable vascularization ($>100 \mu\text{m}$), and transport of important substances. Furthermore, the mechanical properties of the bioimplant should aim at matching the properties of native bone tissue to give support, and simultaneously promote osteogenic differentiation through mechanical stimuli. Additionally, the surface morphology of the bioim-

plant should provide microscale roughness allowing adhesion of cells and tissue formation. Chemically, the implant and possible degradation products should be biocompatible and nontoxic, while being active by promoting bone formation through osteoconductivity and/or osteoinductivity.

The bone regeneration capacity of similar scaffolds has previously been shown *in vitro* using bone marrow mesenchymal stem cells (MSCs)^[10,12] and *in vivo* in rabbits^[10,12] and sheep.^[11] In a calvarial CSD model in rabbits, a neat PTMC-tMA-network scaffold without a bioactivating ceramic component improved bone regeneration by providing a surface for bone growth. Addition of β -TCP or hydroxyapatite (HA) resulted in more dispersed bone formation *in vivo* indicating improved osteoconductivity.^[12] The biocompatibility and osteoconductivity of the PTMC-tMA-network and calcium phosphate composites manufactured by vat photopolymerization are further supported by studies conducted with PTMC-tMA-networks and HA in a calvarial defect in rabbits^[10] and orbital floor reconstruction in sheep.^[11] As a part of this study, prior to conducting the minipig experiment, an *in vitro* cytotoxicity, biocompatibility and bone forming capacity assessment (see Supporting Information) of PTMC and PTMC+TCP was done using MSCs. The analysis showed that cells proliferated well on all materials, showing no signs of cytotoxicity, while a more consistent osteogenic response was seen in the PTMC+TCP bioimplants.

In vivo in minipigs, the interface between the bioimplant and newly formed bone pointed towards successful bioactivation of the PTMC with β -TCP. The composite showed an intimate osseointegration of new bone with the available ceramic at the bioimplant surface without intervening loose connective tissue as seen with the neat PTMC (Figure 8). Furthermore, osteoclasts covering the PTMC+TCP bioimplant surface seemed to induce osteogenesis through the osteoclast-osteoblast coupling mechanism,^[35] pointing towards scaffolds being not only osteoconductive but also osteoinductive. To avoid a confounding osteoinductive effect, we opted to use venous blood for soaking/wetting the bioimplants, as venous blood is not expected to have an osteoinductive effect.^[36]

Nevertheless, the PTMC+TCP bioimplants were associated with a higher incidence of necrosis and infection, of which the pathogenesis is not yet fully clear. It is possible that the large implant with substantial amounts of the β -TCP caused local microenvironmental changes that further led to inflammation and/or tissue damage and local necrosis prone to infection. *In vivo*, dissolution of β -TCP occurs by cell-mediated resorption, where cells provoke a local acidification leading to β -TCP dissolution.^[37] Furthermore, calcium phosphate surface mineralization reactions lead to changes in pH and calcium and phosphate levels creating concentration gradients between the local chemical environment in the implant and outside it.^[38] β -TCP naturally forms apatite *in vivo*, but the formation can also be triggered/accelerated by autoclaving.^[37] Bohner et al.^[39] proposed a mechanism where these microenvironmental changes and especially calcium and/or phosphate depletion result in intrinsic osteoinduction. We speculate that the large size of the highly active porous implant may have led to sub-physiologic pH levels, causing infection. β -TCP in powder form was readily available at the surface of the scaffolds at high volumes and with a large surface area compared to that of, e.g., large granules.

Interestingly, smaller similarly 3D printed composite scaffolds did not cause inflammation or infection in a rabbit calvarial model.^[12] This indicates a caution signal when interpreting pre-clinical results in the context of the tested species, reconstructed bone, and importantly the size of the 3D-printed bioimplant. Another plausible reason for the inflammation is the β -TCP particle size. *In vivo* application of calcium phosphate ceramics has been reported to lead to an early inflammatory response due to macrophage phagocytosis of particles smaller than 5 μm .^[40] Correspondingly, the β -TCP particles utilized in this study ranged from 1 to 10 μm in diameter. Developing the bioimplant we aimed to maximize the content of the bioactive and reinforcing component. Although the bioactivation succeeded as evidenced in osseointegration and new bone formation, our results point towards cautious evaluation of optimal composition and physico-chemical properties of the chosen calcium phosphate grade and perhaps the polymer/ceramic ratio. Further experiments are warranted to address these concerns, especially with the fast-resorbing β -TCP. Alternatively, slower-resorbing calcium phosphate ceramics, such as HA or biphasic calcium phosphates, could be considered. Potentially the slower dissolution would be more favorable in sizable bioimplants in CMF reconstruction. However, this could also be associated with less bioactivation, as β -TCP was chosen as one of the most potent bioactivators.^[37] On the other hand, Chatterjea et al. showed in a critical-sized femoral defect in rats, that both hydroxyapatite (HA) and β -TCP elicited a strong inflammatory response until 12 days postimplantation which subsided gradually through the following 6 weeks.^[41] The polymer/ceramic ratio could be reconsidered to achieve a predictable biological response by targeting essential bioactivation, while minimizing the risk for potential inflammatory reaction.

The bioimplants used within this study were manufactured individually for each minipig according to their anatomy with control over multiple criteria (pore size, porosity, stiffness, surface morphology, bioactive content) that facilitate bone growth. For the manufactured bioimplants, a pore size smaller than the chosen 800 μm would have been preferred, providing a higher surface area and more effective pore bridging. Moreover, smaller pores could improve the wettability of the bioimplant by lowering the surface tension of liquid within the pores, creating a sponge effect for the autologous blood prior to implantation. While the hydrophilic^[14] surface of our bioimplants was easily wetted using blood, they did not retain the blood in the porous structure. A higher level of detail in manufacturing by vat photopolymerization can be achieved with, e.g., decreased strut thickness and pore size. However, when manufacturing large structures at higher resolution, the fragile, swollen structures may have more difficulty to withstand the mechanical forces during the separation of the structure after completing each layer, resulting in an increased risk of failure.

A significant property of manufacturing polymer/ceramic scaffolds using vat photopolymerization resins, including non-reactive solvents, is the surface enrichment of the ceramic particles that occurs as an effect of the solvent extraction and subsequent shrinking of the scaffold.^[10,14] As a result, the bioactive ceramic particles are directly available at the surface of the bioimplant, providing an osteoconductive surface and microscale surface roughness. Another important aspect of utilization of crosslinking polymers, is that the manufactured bioimplants are

sterilizable by autoclaving, which is critical for easier translation and integration into a clinical setting.^[42]

Lack of mechanical stability and micromotions of the implanted constructs can impede new bone formation.^[24] Nevertheless, in our study, there was a direct continuation between the native bone and the newly formed bone within the bioimplants. The new bone formation was largely formed through intramembranous ossification, reflecting the biomechanical stability and the accuracy of the design/manufacturing, as the bioimplants were snugly fitted within the defects without the need for screw fixation. Further, the stiffness of the bioimplants may be altered by varying the β -TCP content, and the addition of the ceramic greatly reinforces the composite as we have previously shown.^[14] In fact, for the purpose intended in this study, the PTMC bioimplant was considered overly flexible, while the semi-rigid PTMC-TCP scaffolds allowed for a close-fitting insertion into the defect.

The patient-specific titanium reconstruction plates utilized to support the mandible performed well throughout the study. Titanium is a well-established material in reconstruction surgery and the medical grade used in the study is known to be biocompatible.^[43] Further proof of the biocompatibility was established within this study as bone was formed also directly on the plate. The reconstruction plate design provided a good fit on the mandible. In addition, resection markings and positioning hooks were included successfully in the virtual design of the resection to guide plate alignment. Since minipig biting forces, mastication and animal ethology loads were largely unknown, plates were designed robust ensuring durability. Thus, no deformations of the plates were found during the study, while some degree of stress shielding was evident. More research is needed to design plates that allow optimal bone growth stimulus without breaking.

On a final note, it could be concluded that the study was overall successful, and the production workflow was effectively applied within the intended timeframe. The PSIs were manufactured at a high build quality for both bioimplants and reconstruction plates with minimal deviations from the virtual design. The implants performed well in the *in vivo* setting, streamlining the surgery. However, some questions regarding the clinical aspects of the bioimplant still remain. Most important is the necrosis and infection occurring in the PTMC+TCP group, raising the question of the best bioactive component for large reconstruction scaffolds in the craniomaxillofacial area. The presented work establishes a platform for optimization and upscaling of PTMC-tMA-network/ceramic 3D-printed composite scaffolds for large maxillofacial bone reconstructions. This will facilitate future studies towards a predictable application in a clinical setting.

5. Conclusions

In this study, hybrid reconstruction implants including bone regeneration bioimplants and supporting titanium plates were engineered for treatment of mechanically demanding mandibular continuity defects. A complete production workflow was tested *in vivo* in minipigs. The study highlights the importance of *in situ* large animal studies for evaluating bone tissue engineering implants, as findings on small animal models do not translate well into large animal models, let alone human clinical applications. Further, while the PTMC-tMA-network itself was biocompatible,

additional research is needed to evaluate the optimal composition of the composite, in terms of calcium phosphate ceramic choice, polymer-ceramic ratio and particle size to be used in large CMF reconstructions. Furthermore, the study sheds light on the requirements in mandibular reconstructions of sizeable continuity defects in minipigs, supporting future studies using this large animal model.

6. Experimental Section

An overview of the study and experimental design is presented in Section 2. The outline of the *in vivo* animal study is presented in Figure 1 and the study groups are shown in Table 1. Surgeries were carried out in two steps. In surgery 1, mandibular molars were removed at the planned defect site, while surgery 2 entailed the actual mandibular resection and implantation. The surgeries and implants were planned in close collaboration with CMF surgeons at Helsinki University Hospital (HUS). The right mandibular body was chosen as the experimental site and the left side remained untreated. The study and surgical protocols were approved by the Finnish Animal Experiment Board (ESAVI/16 103/2018) and the study was conducted according to ARRIVE guidelines (ARRIVE Checklist: see Supporting Information). Surgical interventions in the lower jaw were performed in 12 female minipigs (Ellegaard Göttingen Minipigs, Dalmose, Denmark) age 2.1 ± 0.1 years, weight 37.6 ± 3.5 kg (range 33.9 – 46.3 kg). The animals were selected to be dentally mature and females for smaller teeth. The animals were fasting for 12 hours before surgery, with water accessible *ad libitum*. Surgical procedures were performed under general anesthesia (GA) in aseptic conditions by CMF surgeons from HUS. The animals were monitored regularly, kept on sawdust bedding throughout the experiment, and housed in groups of 3–4 animals per pen.

The animals received perioperative medication, anesthesia, intraoperative monitoring, and analgesia by a specialized veterinarian, following the guidelines of the animal breeders^[44] (Supporting Information). During surgery, blinding was not possible due to obvious differences between the bone segments (positive control) and the bioimplants groups. Subsequent analyses (CT, μ CT, plate deformations, and histological analysis) were performed by independent experts with blinding to the maximum practical extent.

Surgery 1: Teeth Extraction: In the first surgical procedure, erupted or partially erupted mandibular molars (M1-M3) were surgically removed avoiding contact with the oral cavity in subsequent mandibular resection and to reduce occlusal stress on resection site. After local anesthesia (Lidocain c. adrenalin, 20 mg ml⁻¹, Orion Pharma) a buccal mucoperiosteal flap was raised and buccal osteotomies using a round stainless-steel bur were carried out under sterile saline cooling. The molars were sectioned and extracted with dental elevators and forceps. Extraction sockets were curetted and flushed carefully; any sharp bone edges were removed to achieve a good closure. Wounds were closed with resorbable Vicryl 3-0 sutures. The animals were kept on a soft feed diet the remainder of the study. Two weeks postextraction, each animal underwent CT imaging, for designing a PSI, under GA which allowed the verification of healing of the intraoral wound.

Fabrication of Patient-Specific Composite Bioimplants and Plates: The patient-specific composite bioimplant and titanium reconstruction plates were manufactured according to the block diagram described in Figure 2, using pre-operative computed tomography (CT) scans performed after teeth extraction (see Figure 1 for study outline). Each step of this virtual surgery and modeling workflow is described in detail in the following chapters.

Fabrication of Patient-Specific Composite Bioimplants and Plates—Computed Tomography Scanning: CT imaging was performed 6 weeks before biomaterial implantation (pre-op CT, Figure 1). The minipigs were scanned in a prone position under general anesthesia using a combination of ketamine and dexmedetomidine as described above. The CT scan was performed on a LightSpeed VCT 64 slice CT Scanner (GE Medical Systems,

USA). The scan protocol used no contrast enhancement for the bone being a high-contrast tissue. The pre-op CT scan parameters for scanning after teeth extraction were: voltage 120 kV; maximum of 500 mA; slice thickness: 0.625 mm; total detector width 40 mm; rotation speed 0.6 s. After the 2nd surgery, the following parameters were used: voltage 140 kV; maximum 450 mA; slice thickness 0.625 mm; detector width 40 mm, rotation speed 0.7 s.

Fabrication of Patient-Specific Composite Bioimplants and Plates—Modeling and Construction of Porous Bioimplant and Reconstruction Plate: The pre-op CT-scan DICOM data was used to reconstruct a volumetric model with the aid of Slicer 4.10.1 software (www.slicer.org). The bone segments were separated from other tissue by using threshold value HU 400. The applicability of the value was secured adjusting manually the value so that clear noise vanished. Modest Laplacian smoothing was used (20%) to retain detail accuracy. The models were exported as STL files which were transferred for further geometric operations to 3DataExpert, a STL editor software (DeskArtes Oy, Finland).

In 3DataExpert software, the triangular facet mesh was fixed, verified and remaining separate small shells that origin from noise data of DICOM segmentation was cleaned. The models were marked with geometric identification features so that they can securely be identified and connected to the correct study animal. The defect, a 25 mm resection, was virtually cut from the mandible to form the bioimplant shape and volume. Since the minipig mandible was tubular, the cut volume's ends were patched manually using different STL editing techniques to form one solid volume suitable for gyroid conversion and bioimplant 3D printing. To convert the defect into a porous bioimplant, a porous cube with a gyroid structure with the wanted porosity of 71% and pore size 800 μm was generated with mathematical modeling software MathMod (<https://sourceforge.net/projects/mathmod/>). The cube was exported as STL and imported in Blender software (www.blender.org) where a Boolean intersect operation was performed between the solid defect piece cut from the mandible and the porous cube. The resulting porous bioimplant was saved as STL and possible holes in the generated porous bioimplant structure were repaired by using a Default repair script in Netfabb software (Autodesk, USA). A final STL-file was exported for printing.

The reconstruction plates to support the defect were modelled using re-topology technology (RT) of Modo software (The Foundry Visionmongers Ltd, UK). The RT allows to lay patches on imported facet geometry and to model smooth, feature rich geometries. This technology was chosen instead of Boolean operations commonly used in the creation of medical implants because of flexibility, model complexity, and process productivity. The reconstruction plate Y-geometry with positioning hooks and resection markings defined by CMF surgeons through pre-operative models, drawings and spoken instructions were modelled by an expert on the corresponding reconstructed mandible. The screw holes were done using pre-modelled cutter part and Boolean difference operator. The fitting and final geometry of the design was secured by editing and verifying them in 3DataExpert software on virtual mandible 3D models of the same study animal.

Prior to the design and animal study, a finite element (FEM) analysis was performed using a prototype 3D model of the reconstruction plate to estimate required dimensions and strengths, utilizing available information of minipig biting forces and mastication (see Supporting Information).

Fabrication of Patient-Specific Composite Bioimplants and Plates—Fabrication of Patient-Specific Bioimplants: Three-armed poly(trimethylene carbonate) PTMC-tMA was synthesized by ring-opening polymerization and subsequent methacrylation to obtain a photo-crosslinkable macromer as previously described elsewhere^[14] and briefly in the Supporting Information. For manufacturing bioimplants by stereolithography, a resin was prepared by dissolution of PTMC-tMA in propylene carbonate ($\geq 99.0\%$, Merck Millipore) at 40 °C. Photoinitiator Omnirad TPO-L (IGM Resins), and Orasol Orange G (CIBA Specialty Chemicals) dye were added at room temperature. To manufacture composite scaffolds β -tricalcium phosphate (β -TCP, powder, particle size 2–6 μm , $\geq 90\%$ phase purity, Sigma Aldrich) was incorporated into the resin. The used composition for the PTMC-tMA resin was 48.7 wt%

PTMC-tMA, 48.7 wt% propylene carbonate, 2.6 wt% photoinitiator TPO-L and 0.09 wt% dye, while the composite PTMC-tMA+TCP resin included 30.1 wt% PTMC-tMA, 16.2 wt% β -TCP, 1.6 wt% TPO-L, and 0.04 wt% dye. The resin composition optimization for vat photopolymerization has been previously described elsewhere.^[14] In short, the resins must contain enough functionalized polymer to crosslink evenly during the light exposure time of the vat photopolymerization device and the resin needs to flow well enough to fill the gap between the build plate and previously crosslinked layer between the crosslinking cycles. The light penetration depth into the resin, and thereby the thickness of the crosslinked layer, is controlled by adding a dye to the resin according to a working curve.^[14]

The patient-specific bioimplants were manufactured by vat photopolymerization with a Perfactory III Mini SXGA+ digital light processing stereolithography device (Envisiontec, Germany) using the resins described above. Each CAD file was scaled to account for the swelling caused by the propylene carbonate present in the resin. The printing was performed at a light intensity of 700 mW dm^{-2} and a wavelength of 400–550 nm while exposing each layer for 12 s. The layer thickness used was 50 μm . During a solvent extraction with ethanol postprinting, the scaffolds were allowed to shrink isotropically to their final size.^[14] Following removal of propylene carbonate and residual resin during the thorough extraction the scaffolds were washed with ethanol ($\geq 99.5\%$, Etax Aa, Altia Industrial) for three days while changing the ethanol daily. The scaffolds were dried in vacuum at 40 °C until constant weight. The technical details regarding printing are described in more detail in a previous publication covering material property characterization of similar scaffolds.^[14]

To characterize the ceramic content in the final implants, thermogravimetric analysis (TGA) was performed using a TGA Q500 device (TA Instruments, USA) by heating at a rate of 10 °C min^{-1} to 600 °C while monitoring mass change. A Hitachi TM-1000 scanning electron microscope (SEM) was utilized to image the surface features of PTMC and PTMC+TCP scaffolds. The bioimplants were autoclaved prior to implantation at 134 °C for 20 min with pulse drying where the chamber was alternatively pressurized and depressurized.

Fabrication of Patient-Specific Composite Bioimplants and Plates—Fabrication of Patient-Specific Reconstruction Plate: The reconstruction plates were manufactured by Proto labs Ltd. (Shropshire, UK). The manufacturing technology was laser powder bed fusion (L-PBF, ISO/ASTM:52 900) and material was medical grade titanium (Ti 6Al-4V, 30 μm layers). Ajatec Oy (Finland), a local dealer of Proto Labs Ltd, was used for faster lead time of the order process. Each mandible 3D model was printed with uPrint 3D printer (Stratasys Ltd, Israel/USA) using ABS plastic for pre-operative planning and titanium plate fitting. The screw holes, designed to have tight tolerance, were cleaned with hand drilling to remove the surface roughness. The plates were autoclaved at 134 °C for 20 min with pulse drying.

Surgery 2: Mandibular Resection and Reconstruction Using Bioimplant and Plate: The animals were randomly assigned to each study group (Table 1). In the second surgery, a 25 mm long continuity defect was created in the right mandibular body region. The defects had a volume of $8.6 \pm 1.1 \text{ cm}^3$. After local anesthesia (lidocaine with epinephrine), sterile skin cleansing, and sterile coverings resection site was exposed through sub-mandibular approach. The patient-specific reconstruction plate was fit into place and attached temporarily with a few screws and all drill holes were pre-drilled. The resection area was marked with a pencil on the bone according to resection markings on the plate. Then the plate was removed, and resection was performed by oscillating bone saw (Stryker). The excised bone pieces were kept in 10% neutral buffered formalin and analyzed with μCT . Reconstruction according to study design was conducted and all plates were stabilized with 15 bicortical screws (10 and 20 mm) in each plate to achieve rigid fixation of the mandibular segments. Figure 5 shows the placement of the screws. The mandibular continuity defects were either reconstructed using the 3D printed patient-specific bioimplants, modified native bone segments, or left empty as negative controls. The bioimplants were soaked with autologous blood prior to implantation. During the surgery, contact with the oral cavity was strictly avoided. A proper hemostasis was achieved by bipolar and ligatures. Drainage was not used. The periosteum and subcutaneous tissue were closed with re-

resorbable 3-0 Vicryl sutures, skin closure performed with intracutaneous resorbable monofilament Monocryl sutures.

Timepoint and Experiment End Point Analysis: During the study, two timepoints at 6 and 16 weeks CT scans were performed. Prior to the last CT scan 24 weeks postimplantation, the animals were euthanized. The defect site in mandible was harvested, examined and prepared for μ CT analysis and histological processing. Furthermore, the reconstruction plates were collected for mechanical verification scanning.

Timepoint and Experiment End Point Analysis—Computed Tomography Analysis: To evaluate the dynamics of new bone formation, CT scans of the skull was performed 6 weeks before biomaterial implantation (pre-op CT, Figure 1) and at 6, 16, and 24 weeks postimplantation. During CT analysis at 6 and 16 weeks, the animals were under general anesthesia as described previously. Prior to final CT at 24 weeks the animals were euthanized. The CT data from all time points were evaluated by a blinded veterinary radiologist and subjectively scored for ossification and callus formation.

Timepoint and Experiment End Point Analysis—Microcomputed Tomography: At 24 weeks postimplantation, the defect site in each mandible was harvested as a block with a 1 cm rim of original bone both anteriorly and posteriorly, examined macroscopically and fixed with 4% paraformaldehyde (PFA). Next, μ CT analysis was performed using a GE phoenix nanotom[®] s system (General Electric Sensing and Inspection Technologies/Phoenix X-ray, Germany) at the University of Helsinki X-Ray Micro-CT Laboratory. The samples were imaged at 45.7 μ m voxel size, with X-ray generator settings at 80 kV and 200 μ A, using a 1 mm Al filter. A total of 1800 projection images were recorded over a 360-degree rotation of the sample with 5 \times 250 ms exposure time for each projection. The 3D volume data was reconstructed using Bruker NRecon version 1.6.10.2 (Bruker, Belgium).

Data series were re-oriented using DataViewer software (Bruker, Belgium) to have the consistently aligned coronal sections of the samples for downstream registration of volume of interest (VOI) and subsequent quantitative analysis. In CT Analyzer (CTAn) software (Bruker, Belgium) the VOIs were registered corresponding to the reconstructed defect with a 0.5–1.0 mm rim of the former defect edges both anteriorly and posteriorly. Two VOIs were determined for PTMC and PTMC+TCP groups, with one VOI including only the bioimplant to assess the bone growth within the scaffolds and a second VOI including all bone within the defect site. For distinguishing the newly formed bone from the bioimplant and soft tissue, a constant grey value threshold of 140 was applied across all samples. Bone volume (BV) within the VOIs was determined using the 3D analysis script in CTAn software. The BV of the new bone within the defect was compared to the original BV of the defect and total volume (TV) of the defect site received from pre-op CT analysis after teeth extraction. For this comparison, the width of the original defect was matched with the width analyzed for the μ CT data. For visualization of the formed bone within the defect site and the implant 3D reconstructions were exported from CTAn software and rendered in Blender software.

Timepoint and Experiment End Point Analysis—Histological Analysis: The mandibular samples were fixed in 10% neutral buffered formalin (NBF), scanned with μ CT and subsequently processed for histology. For paraffin embedded histology, parts of the mandibular samples (see Figure 7) continued fixation for 10 days and were then decalcified in 0.5 M Ethylenediaminetetraacetic acid (EDTA) 7.5 pH for 12 weeks, dehydrated in ascending alcohol series, cleared in xylene and embedded in paraffin. Serial tissue sections with 4 μ m thickness were prepared from the mid-sagittal plane of the defect area, treated with hematoxylin-eosin, Masson Trichrome (MT) and Gram stain, then observed under a light microscope (Carl Zeiss Inc., Germany). Both temporomandibular joints (TMJ) from all animals were also collected and were EDTA-decalcified. The animals were autopsied, and samples were collected for assessment of tissue response to bioimplants (Supporting Information). Slides were digitalized using a Panoramic 250 FLASH II digital slide scanner (3DHISTECH, Hungary) at Genome Biology Unit, University of Helsinki.

The hard tissue histology was performed on parts of the mandibular sample by BioSiteHisto Oy (Finland) Briefly, the harvested bone blocks were fixed in 10% NBF, dehydrated in ascending alcohol series, cleared in

xylene, and embedded gradually into methyl methacrylate (MMA). Then, 5 μ m thin slices were sectioned from the center of the defect using a hard tissue microtome Leica SM2500 Sectioning System (Leica Biosystems, USA), collected on albumin-glycerin coated slides. To improve adherence of the sections to slides, they were heated at 60 $^{\circ}$ C for 3–5 days after sectioning. The sections were then stained employing modified MT staining. Slides were digitalized as WSI in Mirax format with a 3DHistech Panoramic MIDI scanner (3DHISTECH, Hungary) by BioSiteHisto Oy.

Timepoint and Experiment End Point Analysis—Reconstruction-Plate Geometry Validation: The reconstruction plates were scanned using industrial grade ATOS core 3D scanner (GOM GmbH, Germany) before and after the use in the animal study. This was to find possible deformations during the manufacturing process and after in vivo use. Markers were attached on the plates to enable joining of different scan exposures and plates were rotated under structural light scanner till the geometry was captured from all sides. The geometries were compiled and cleaned with GOM Scan V8 software (GOM GmbH, Germany). Both scans, referred to as *Built* and *postoperative*, were compared to the original design model (*as-Designed*) in CloudCompare open-source software (www.cloudcompare.org) by aligning the models and analyzing the dimensional differences resulting in a Gaussian mean.

Supporting Information

Supporting Information is available from the Wiley Online Library or from the author.

Acknowledgements

A.A.-S and R.K. contributed equally to this work as first authors. R.S.-K, J.S., and B.M. contributed equally to this work as senior authors. The project was funded by Business Finland (CraMaxS 557/31/2016) and was implemented in collaboration between University of Helsinki, Aalto University, and Helsinki University Hospital in cooperation with Planmeca Oy, DeskArtes Oy, Versoteq 3D Solutions Oy, and Labquality Oy. Additional funds from the in vivo study were also received from Helsinki University Hospital State funding for university-level health research (Grant Nos. Y1149SUL30, Y1014SL015, Y1014SULE1, TYH2018225, and TYH2019117). The authors kindly thank Stryker Ltd for craniomaxillofacial instrumentation used in surgical procedures, Dr. Heikki Suhonen X-Ray Micro-CT Laboratory for μ CT expertise, staff at Large Animal Center for animal care, Veterinary Teaching Hospital for CT imaging, Finnish Centre for Laboratory Animal Pathology (FCLAP) for histopathological services and Genome Biology Unit for histology scanning, and all part of HiLIFE University of Helsinki. Ashish Mohite from Aalto University School of ARTS supported the research with modelling expertise. This work made use of Aalto University Bioeconomy Facilities.

Conflict of Interest

The authors declare no conflict of interest.

Data Availability Statement

The data that support the findings of this study are available from the corresponding author upon reasonable request.

Keywords

additive manufacturing, bone reconstructions, calcium phosphates, continuity defects, Göttingen minipigs, poly(trimethylene carbonate)

Received: October 4, 2021
Revised: December 15, 2021
Published online:

- [1] S. Järvinen, J. Suojanen, E. Kormi, T. Wilkman, A. Kiukkonen, J. Leikola, P. Stoor, *J. Cranio-Maxillofacial Surg.* **2019**, *47*, 1072.
- [2] H. Qu, H. Fu, Z. Han, Y. Sun, *RSC Adv.* **2019**, *9*, 26252.
- [3] E. D. Roumanas, N. Garrett, K. E. Blackwell, E. Freymiller, E. Abemayor, W. K. Wong, J. Beumer, K. Fueki, W. Fueki, K. K. Kapur, *J. Prosthet. Dent.* **2006**, *96*, 289.
- [4] H. Schliephake, F. W. Neukam, R. Schmelzeisen, B. Varoga, H. Schneller, *J. Cranio-Maxillofacial Surg.* **1995**, *23*, 243.
- [5] N. Mardas, X. Dereka, N. Donos, M. Dard, *J. Invest. Surg.* **2014**, *27*, 32.
- [6] M. Dang, L. Saunders, X. Niu, Y. Fan, P. X. Ma, *Bone Res.* **2018**, *6*, 25.
- [7] S. J. Hollister, *Nat. Mater.* **2005**, *4*, 518.
- [8] F. P. W. Melchels, K. Bertoldi, R. Gabbrielli, A. H. Velders, J. Feijen, D. W. Grijpma, *Biomaterials* **2010**, *31*, 6909.
- [9] X. Yu, X. Tang, S. V. Gohil, C. T. Laurencin, *Adv. Healthcare Mater.* **2015**, *4*, 1268.
- [10] O. Guillaume, M. A. Geven, C. M. Sprecher, V. A. Stadelmann, D. W. Grijpma, T. T. Tang, L. Qin, Y. Lai, M. Alini, J. D. De Bruijn, H. Yuan, R. G. Richards, D. Eglin, *Acta Biomater.* **2017**, *54*, 386.
- [11] O. Guillaume, M. A. Geven, V. Varjas, P. Varga, D. Gehweiler, V. A. Stadelmann, T. Smidt, S. Zeiter, C. Sprecher, R. R. M. Bos, D. W. Grijpma, M. Alini, H. Yuan, G. R. Richards, T. Tang, L. Qin, L. Yuxiao, P. Jiang, D. Eglin, *Biomaterials* **2020**, *233*, 119721.
- [12] A. Kumar, A. K. Teotia, K. Dienel, I. Qayoom, B. Van Bochove, S. Gupta, J. Partanen, J. Seppälä, *ACS Appl. Mater. Interfaces* **2020**, *12*, 48340.
- [13] J. J. Rongen, B. Van Bochove, G. Hannink, D. W. Grijpma, P. Buma, *J. Biomed. Mater. Res., Part A* **2016**, *104*, 2823.
- [14] K. E. G. Dienel, B. Van Bochove, J. V. Seppälä, *Biomacromolecules* **2020**, *21*, 366.
- [15] A. Barbas, A.-S. Bonnet, P. Lipinski, R. Pesci, G. Dubois, *J. Mech. Behav. Biomed. Mater.* **2012**, *9*, 34.
- [16] G. He, P. Liu, Q. Tan, *J. Mech. Behav. Biomed. Mater.* **2012**, *5*, 16.
- [17] G. He, P. Liu, Q. Tan, G. Jiang, *J. Mech. Behav. Biomed. Mater.* **2013**, *28*, 309.
- [18] K. A. Maratea, P. W. Snyder, G. W. Stevenson, *Vet. Pathol.* **2006**, *43*, 447.
- [19] J. Aerssens, S. Boonen, G. Lowet, J. Dequeker, *Endocrinology* **1998**, *139*, 663.
- [20] J. Aerssens, J. Dequeker, J. M. Mbuyi-Muamba, *Clin. Rheumatol.* **1994**, *13*, 54.
- [21] G. Corte, *Comparative Cephalometric Studies of the Mandible in Growing Göttingen Minipigs Using 3D Computed Tomography: Refining Experimental Dental and Orofacial Research (Doctoral Dissertation)*, Freien Universität Berlin, **2020**.
- [22] J. A. MCGovern, M. Griffin, D. W. Huttmacher, *Dis. Models Mech.* **2018**, *11*, dmm033084.
- [23] J. C. Reichert, S. Saifzadeh, M. E. Wullschlegler, D. R. Epari, M. A. Schütz, G. N. Duda, H. Schell, M. Van Griensven, H. Redl, D. W. Huttmacher, *Biomaterials* **2009**, *30*, 2149.
- [24] S. Konopnicki, B. Sharaf, C. Resnick, A. Patenaude, T. Pogal-Sussman, K. G. Hwang, H. Abukawa, M. J. Troulis, *J. Oral Maxillofac. Surg.* **2015**, *73*, 1016.
- [25] B. Ruehe, S. Niehues, S. Heberer, K. Nelson, *Oral Maxillofac. Surg. Oral Maxillofac. Implant* **2009**, *108*, 699.
- [26] H. F. Marei, K. Mahmood, K. Almas, *Implant Dent.* **2018**, *27*, 135.
- [27] K.-O. Henkel, V. Bienengraber, S. Lenz, T. Gerber, *Key Eng. Mater.* **2005**, *284*, 885.
- [28] M. Dau, P. W. Kämmerer, K.-O. Henkel, T. Gerber, B. Frerich, K. K. H. Gundlach, *Clin. Oral Implants Res.* **2016**, *27*, 597.
- [29] K.-O. Henkel, T. Gerber, S. Lenz, K. K. H. Gundlach, V. Bienengraber, *O. Surgery, Oral Maxillofac. Surg.* **2006**, *102*, 606.
- [30] J.-L. Ma, J.-L. Pan, B.-S. Tan, F.-Z. Cui, *J. Tissue Eng. Regener. Med.* **2009**, *3*, 615.
- [31] N. Ihan Hren, M. Miljavec, *Int. J. Oral Maxillofac. Surg.* **2008**, *37*, 1111.
- [32] S. Rai, V. Rattan, S. S. Jolly, V. K. Sharma, M. M. Mubashir, *J. Maxillofac. Oral Surg.* **2019**, *18*, 224.
- [33] I. Chatzistefanou, S. Kabesi, K. Paraskevopoulos, D. Kolioukas, K. Antoniadis, *Int. J. Clin. Pediatr. Dent.* **2016**, *9*, 273.
- [34] M. A. Geven, D. W. Grijpma, *Multifunct. Mater.* **2019**, *2*, 024003
- [35] N. A. Sims, T. J. Martin, *Annu. Rev. Physiol.* **2020**, *82*, 507.
- [36] S. Spalthoff, R. Zimmerer, J. Dittmann, H. Kokemüller, M. Tiede, L. Flohr, P. Korn, N.-C. Gellrich, P. Jehn, *Regener. Biomater.* **2018**, *5*, 77.
- [37] M. Bohner, B. L. G. Santoni, N. Döbelin, *Acta Biomater.* **2020**, *113*, 23.
- [38] Y. Maazouz, I. Rentsch, B. Lu, B. L. G. Santoni, N. Doeblin, M. Bohner, *Acta Biomater.* **2020**, *102*, 440.
- [39] M. Bohner, R. J. Miron, *Mater. Today* **2019**, *22*, 132.
- [40] F. Peters, D. Reif, *Materialwiss. Werkstofftech.* **2004**, *35*, 203.
- [41] A. Chatterjea, J. Van Der Stok, C. B. Danoux, H. Yuan, P. Habibovic, C. A. Van Blitterswijk, H. Weinans, J. De Boer, *J. Biomed. Mater. Res., Part A* **2014**, *102*, 1399.
- [42] C. Garot, G. Bettega, C. Picart, *Adv. Funct. Mater.* **2021**, *31*, 2006967.
- [43] J. T. Tuomi, R. V. Björkstrand, M. L. Pernu, M. V. J. Salmi, E. I. Huotilainen, J. E. H. Wolff, P. K. Vallittu, A. A. Mäkitie, *J. Mater. Sci.: Mater. Med.* **2017**, *28*, 53.
- [44] A. K. O. Alstrup, *Anaesthesia and Analgesia in Ellegaard Göttingen minipigs*, Ellegaard Göttingen Minipigs A/S, Aarhus, Denmark **2010**.